Energetics and kinetics of vacancy defects in 4H-SiC

Rodrick Kuate Defo, Xingyu Zhang, David Bracher, Gunn Kim, Evelyn Hu, and Efthimios Kaxiras

Energetics and kinetics of vacancy defects in 4H-SiC

Rodrick Kuate Defo,[1] Xingyu Zhang,[2] David Bracher,[2]

Gunn Kim,[3] Evelyn Hu,[2] and Efthimios Kaxiras[1,2]

[1]*Department of Physics, Harvard University, Cambridge, MA 02138, USA.*

[2]*John A. Paulson School of Engineering and Applied Sciences,*

Harvard University, Cambridge, MA 02138, USA.

[3]*Department of Physics, Sejong University, Seoul, 143-747, Korea.*

(Dated: August 21, 2018)

Abstract

Defect engineering in wide-gap semiconductors is important in controlling the performance of single-photon emitter devices. The effective incorporation of defects depends strongly on the ability to control their formation and location, as well as to mitigate attendant damage to the material. In this study, we combine density functional theory (DFT), molecular dyamics (MD), and kinetic Monte Carlo (kMC) simulations to study the energetics and kinetics of the silicon monovacancy (V_{Si}) and related defects in 4H-silicon carbide (SiC). We obtain the defect formation energy for V_{Si} in various charge states and use MD simulations to model the ion implantation process for creating defects. We also study the effects of high-temperature annealing on defect position and stability using kMC and analytical models. Using a larger (480-atom) supercell than previous studies, we obtain the temperature-dependent diffusivity of V_{Si} in various charge states and find significantly lower barriers to diffusion than previous estimates. In addition, we examine the recombination with interstitial Si and conversion of V_{Si} into $C_{\mathrm{Si}}V_{\mathrm{C}}$ during annealing, and propose methods for using strain to reduce changes in defect concentrations. Our results provide guidance for experimental efforts to control the position and density of V_{Si} defects within devices, helping realize their potential as solid-state qubits.

I. INTRODUCTION

Numerous applications of the nitrogen-vacancy (NV) center in diamond for quantum sensing[1] and information science[2] have sparked interest in defect centers in diamond[3] and other wide-bandgap semiconductors such as silicon carbide[4]. SiC is particularly interesting, being a polymorphic material with mature microfabrication and growth techniques[5], which allow access to a variety of emitters with a broad range of emission wavelengths. Spin active and optically active defects in SiC include divacancies[6] in three common polytypes[7], 4H-, 6H-, and 3C-SiC, as well as the negatively charged **silicon monovacancy**[8,9] (V_{Si}^{-}) **in 4H-, 6H- and 15R-SiC**; these defects have long coherence times that persist up to room temperature[6,7,10]. We examine here the V_{Si}^{-} in 4H-SiC, which has optically detected magnetic resonance demonstrated at the ensemble[11] and single-defect level[10], and for which protocols have been proposed for a spin-photon interface[12] and strain and temperature sensing[13]. **The V_{Si}^{-} in 4H-SiC has a spin-3/2 ground state**[12] **which can readily be spin-polarized with incident light and the polarization can be read out through the luminescence**[14], **rendering it usable as a qubit.** As in the case of NV centers in diamond, it is important to increase the photon count rates for V_{Si}^{-}, for instance, by using solid immersion lenses to improve collection efficiency[10] or optical cavities for emission enhancement[15]. Using photonic crystal cavities in 4H-SiC, it has been demonstrated that it is possible to achieve emission enhancement by a factor of ∼80 of the V_{Si}^{-} zero-phonon transition[15]. However, even greater enhancement is expected with improved emitter-cavity coupling. This requires improved control of defect position within a cavity, which necessitates better understanding of the energetics and kinetics of V_{Si}^{-} within 4H-SiC.

This paper describes the use of computational models to study the formation, stability, and kinetics of defects in the context of experimental techniques such as **ion implantation**[16–18] and thermal annealing[19] used to incorporate V_{Si}^{-} within devices. Specifically, we obtain formation energies of V_{Si}^{-} and related point defects, as well as barriers for diffusion and conversion of V_{Si}^{-} to $C_{\mathrm{Si}}V_{\mathrm{C}}$. These parameters are essential for identifying mechanisms to reduce the density of V_{Si}^{-} toward single-defect quantum information applications or to increase their density for ensemble quantum sensing[20]. The paper is organized as follows: section II describes the computational methods, section III includes the key results and discussion and section IV contains our conclusions.

II. COMPUTATIONAL METHODS

We performed first-principles density functional theory (DFT) calculations for the various defect structures using the VASP code[21–23]. For the exchange-correlation energy of electrons we use the gen-

eralized gradient approximation (GGA), as parametrized by Perdew, Burke and Erzenhof (PBE)[24]. The atomic positions were relaxed until the magnitude of the Hellmann-Feynman forces was smaller than 0.01 eV·Å^{-1} on each atom and the lattice parameters were concurrently relaxed. The wavefunctions were expanded in a plane wave basis with a cutoff energy of 500 eV and a zone-centered grid of $12 \times 12 \times 6$ k-points was used for integrations in reciprocal space for the stoichiometric primitive unit cell. The relaxed lattice parameters of the stoichiometric primitive unit cell were then used for all other structures. Increasing the grid to $24 \times 24 \times 12$ causes a change in the total energy of less than 10^{-4} eV and a change in the lattice constants of less than 10^{-5} Å, while increasing the cutoff energy to 600 eV causes a change in the total energy of less than 10^{-2} eV and a change in the lattice constants of less than 10^{-2} Å. Formation energies and transition states were obtained using a supercell with 480 atoms ($5 \times 6 \times 2$ multiple of the primitive unit cell) with appropriately scaled k-point grids and a cutoff energy of 400 eV.

For the structural features of 4H-SiC, we obtain $a = 3.094$ Å and $c = 10.128$ Å for the in-plane and out-of-plane lattice constants, respectively. This agrees well with experimental values[25] of $a = 3.073$ Å and $c = 10.053$ Å. The formation energies of $V_{\mathrm{Si}}^{(q)}$ in various charge states were obtained from,

$$E_f(q) = E_{\mathrm{def}}(q) - E_0 - \sum_i \mu_i n_i + q(E_{\mathrm{VBM}} + E_{\mathrm{F}}) + E_{\mathrm{cor}}(q) \qquad (1)$$

where q denotes the charge state, with $q \in [-2, +2]$, $E_{\mathrm{def}}(q)$ is the total energy for the defect supercell with charge q, E_0 is the total energy for the stoichiometric neutral supercell, μ_i is the chemical potential of atom i, n_i is a positive (negative) integer representing the number of atoms added (removed) from the system relative to the stoichiometric cell, E_{VBM} is the absolute position of the valence band maximum, E_{F} is the position of the Fermi level with respect to the valence band maximum (generally treated as a parameter) and $E_{\mathrm{cor}}(q)$ is a correction term to account for the finite size of the supercell when performing calculations for charged defects[26]. **Depending on the preparation conditions of 4H-SiC, which may be Si-rich or C-rich, the chemical potential μ_{X} will be given either by $\mu_{\mathrm{X}} = \mu_{\mathrm{X}}^{\mathrm{bulk}}$ or $\mu_{\mathrm{X}} = \mu_{\mathrm{SiC}}^{\mathrm{bulk}} - \mu_{\mathrm{Y}}$ (X, Y $\in$ {C, Si}, X $\neq$ Y) for X or Y-rich preparation conditions, respectively. To illustrate the level of convergence in our results, in Fig. 1 we show a representative case, namely the formation energy of the negatively charged Si vacancy, V_{Si}^{-}, in Si-rich preparation conditions as a function of supercell size, and the correction energy for the supercell containing 256 atoms.** This comparison shows that the correction brings the result close to the limit of the infinite size cell, which is represented reasonably well by the 576-atom supercell.
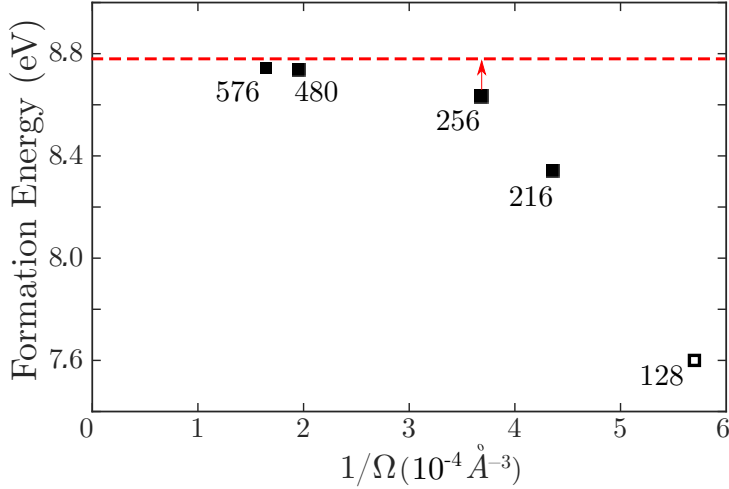
3

FIG. 1. The convergence of the formation energy for V_{Si}^{-} at the k site as a function of the inverse volume of the supercell for sizes of 216, 256, 480 and 576 atoms. The correction for the 256-atom supercell is indicated by the red dashed line: it gives a value for the formation energy of 8.78 eV. The smallest size cell (128) result, indicated by an open square, is from earlier work[27].

The structure of the V_{Si} defect is shown in Fig. 3(a). To further establish convergence of our results, we show in Fig. 3(b) the differences in charge density for two important defects, V_{Si}, and the C vacancy (V_C) combined with a substitutional defect (C_{Si}). The latter defect complex, $C_{Si}V_C$, is the result of displacement of a C neighbor of the V_{Si} into the vacant Si site, and thus related to the diffusion of V_{Si}. These charge density differences are defined as:

$$\Delta\rho(V_{Si}) = \rho(V_{Si}^{-}) - \rho(V_{Si}), \qquad \Delta\rho(C_{Si}V_C) = \rho(C_{Si}V_C^{+1}) - \rho(C_{Si}V_C). \tag{2}$$

These plots show that the charge in the system is well localized near the defect lattice site and well within the boundaries of the defect supercell. Additionally, the charge density differences establish that the redistribution of charge to passivate dangling bonds is consistent with the symmetry of the respective defects, specifically, C_{3v} symmetry in the case of V_{Si}.

As a full *ab-initio* simulation is too computationally intensive for dynamical processes, we carried out classical molecular dynamics (MD) simulations using the LAMMPS package[28,29] with the Tersoff/ZBL potential[30,31] to model the implantation of Si^{+2}, the ion species used in the demonstration of controllably positioning single V_{Si}. Three trials each were done at the angles 10° or 45° to the c-axis at 70 keV and defect numbers were obtained from averages over the three trials. The simulation cell size was $110{\times}67{\times}110$ nm^3 (77 million atoms) for all angles.

For quantifying diffusion, the diffusivity, D, is given by

$$D = \nu_0 d^2 e^{-\varepsilon_b/k_B T} \tag{3}$$

where $\nu_0 = \nu_0(T)$ is the attempt frequency, d is the migration distance, in the case of V_{Si} equal to the second-nearest neighbor hop between Si sites, and ε_b is the activation energy barrier. From harmonic transition-state theory, we calculate the attempt frequency as[32],

$$\nu_0 = \frac{k_B T}{h} \prod_{j=1}^{m'} \frac{e^{-h\nu_j'/2k_B T}}{(1 - e^{-h\nu_j'/k_B T})} \left(\prod_{j=1}^{m} \frac{e^{-h\nu_j/2k_B T}}{(1 - e^{-h\nu_j/k_B T})} \right)^{-1}, \tag{4}$$

where m, m' and ν_j, ν_j' are the corresponding number of normal modes and phonon frequencies, respectively, at the initial (I) and saddle-point (S) configurations (there is one fewer normal mode at the saddle point than at the equilibrium configuration, $m = m' + 1$). To obtain the phonon frequencies, we diagonalize a Hessian matrix, which is symmetric and therefore requires $(m^2 + m)/2$ calculations to obtain all independent matrix elements, at each configuration.

The $V_{\text{Si}}^{(q)}$ defects can migrate through the pathways illustrated in Fig. 2(a). There are two types of pathways, referred to as "eclipsed" when the nearest-neighbor C atoms to the V_{Si} in its original and final positions differ by only a translation by a lattice vector, or "staggered" when they differ by a translation by a lattice vector and a rotation by 60° about the c-axis, respectively. Conversion of the $V_{\text{Si}}^{(q)}$ to $\text{C}_{\text{Si}} V_{\text{C}}^{(q)}$ is also possible through pathways such as the one illustrated in Fig. 2(b), where the C atom from a cubic (k) site replaces the V_{Si} at a k site leaving a vacancy at a k site. The other option we have explored is the conversion $k \rightarrow k, h$, where the V_{Si} at a k site is replaced by a C atom from a hexagonal (h) site, leaving a vacancy at an h site. Based on previous work[27], we do not expect the other possibilities to yield very different results.

Though the energy barriers and attempt frequencies contain all the information necessary to characterize the kinetics of the system, properly computing the diffusion length and the diffusivity requires a kinetic Monte Carlo (kMC) simulation. For the simulation, the transition rates D/d^2 were first accumulated in a vector, then a random number was chosen and the corresponding transition selected. Only silicon vacancies were allowed to transition, an approximation based on our finding of higher transition barriers for all other defect species. The atomic positions were then updated and a second ran-
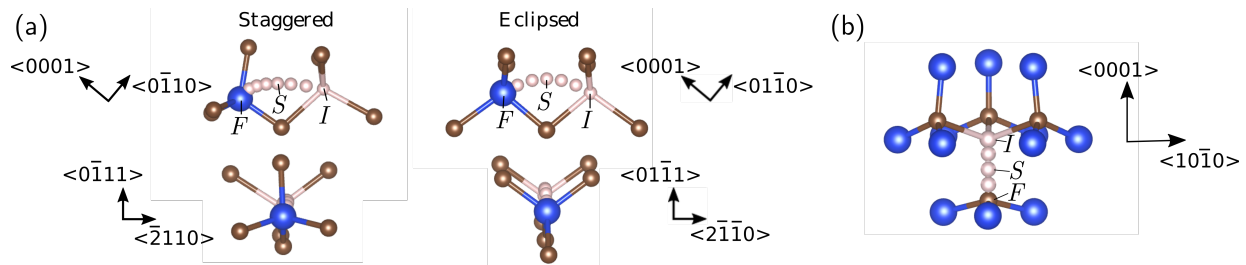
FIG. 2. (a) V_{Si} migration pathways for out-of-plane staggered and eclipsed configurations viewed along two different directions. (b) Pathway for the conversion of V_{Si} to $C_{Si}V_C$. The labeled arrows show the crystallographic axes. The initial (I), saddle-point (S) and final (F) vacancy positions are identified.

dom number selected and the time updated according to an exponential distribution consistent with the memoryless and other physical properties of these transitions.

III.   RESULTS AND DISCUSSION

A key issue in characterizing a system involving lattice defects is the thermodynamic stability and relative populations of defects which are determined by the defect formation energies. The formation energies of defect species considered in our work are summarized in Fig. 4. These show the stability of V_{Si} relative to other complexes, in particular $C_{Si}V_C$, another single photon emitter in 4H-SiC[33], to which the V_{Si} can transform under certain conditions discussed below. **The bandgap used here is a value obtained from DFT and is therefore an underestimation. In particular, we miss the $(0|-2)$ charge transition level[34,35] for V_C, where the occupation level going from q to q' charge states is labelled as $(q|q')$. As the focus of our work is the charge states that can exist with V_{Si}^-, to determine for example the propensity to attachment of V_{Si}^- to V_C, and since our computations fully explore the V_{Si}^- Fermi level regime, we feel that the behavior of the formation energy of V_C beyond the DFT gap is somewhat extraneous to the discussion.** The carbon vacancy (V_C), another well-studied point defect in 4H-SiC[36–38], has a lower formation energy than V_{Si}. However, its unfavorable optical properties (lack of optically detected magnetic resonance) limit its usefulness as a qubit candidate. For nonequilibrium processes such as ion implantation discussed below, the relative formation energies do not give the complete picture for the prevalences of different defect species. Nonetheless, since the formation energies reflect the energy required to break and form bonds for defect complexes, the results in Fig. 4 are consistent with the general trends observed in the MD simulations.

In addition to natural incorporation during growth, controlled by the value of the formation energy, defects may be created in 4H-SiC using electron[10], neutron[19], or proton[11] irradiation, as well as **ion**
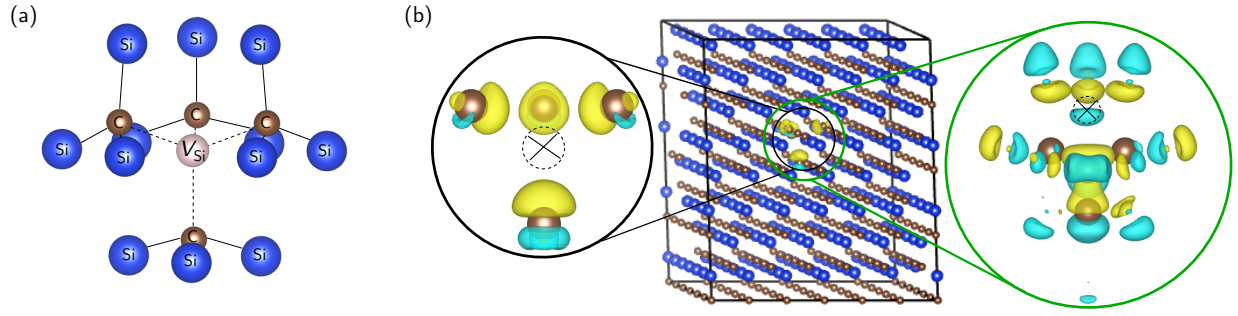
FIG. 3. (a) Structure of the atomic neighborhood around the V_{Si} defect in 4H-SiC. (b) Charge density difference plots, $\Delta\rho(V_{Si})$ (left) and $\Delta\rho(C_{Si}V_C)$ (right), defined in Eq. (2). The location of the vacancy in each case is indicated by a circle in dashed line with a cross inscribed. C atoms are brown and Si atoms blue. Yellow (cyan) isosurfaces indicate electron accumulation (depletion). The rectangular box shows the 576-atom unit cell.
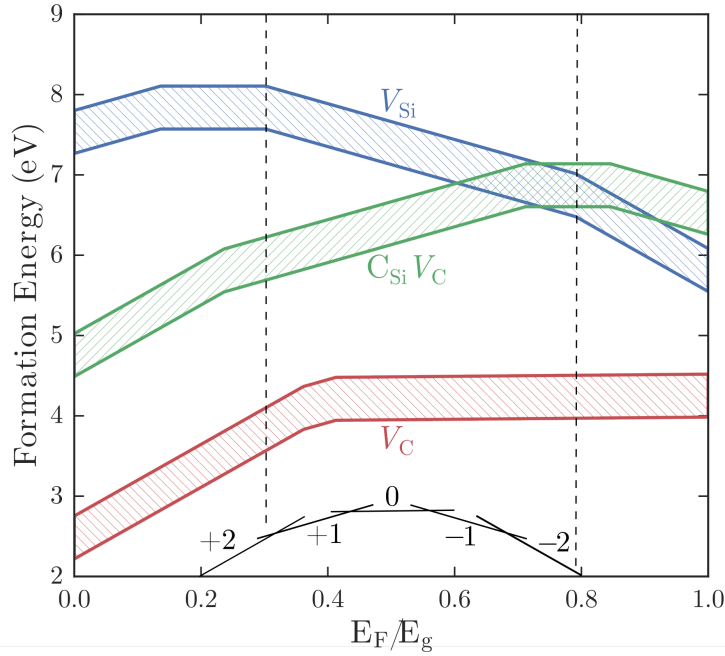

FIG. 4. Formation energy of various defects as a function of the Fermi level in the gap (E_g= 2.23 eV) for the unit cell with 480 atoms: blue lines delineate V_{Si} at cubic (k) sites [results for V_{Si} at hexagonal (h) sites are not shown given a difference of less than 5%]; green lines delineate formation energies for $C_{Si}V_C$; red for V_C. For V_{Si} and $C_{Si}V_C$ the upper (lower) limit of the range corresponds to Si-rich (C-rich) conditions. The opposite is true for V_C. The slopes of the lines denote the charge state as indicated by the labeled black lines in the legend at the bottom. Dashed lines indicate the regime where $q = -1$ is favored for V_{Si}.

implantation[16–18]. In particular, focused ion beam implantation has been used to demonstrate creation of single V_{Si} at **deterministic positions**[17,18], which is needed for their integration within photonic devices. **With MD simulations, we observe channeling at high implantation energies and certain angles, as shown in Fig. 5, where v_x, the velocity along a particular**

in-plane direction, does not decrease as much as the v_z, the velocity along the out-of plane direction, over time, suggesting that the ion is traveling along a channel in the v_x direction. This observation demonstrates the usefulness of this method over binary collision models, which do not include crystal structure and hence cannot show effects such as channeling. Channeling can also be useful for the creation of V_{Si} more deeply within the material, which might have beneficial effects such as improving emitter-cavity coupling in optical devices.

The number of defects formed, averaged over three trials, can be found in Fig. 5 (c). As the ion passes through the cell in the majority of the trials, comparisons are made neglecting defects formed after a cutoff time. This cutoff time is set at the overall minimum time before an ion exits the cell and thus the number of defects formed represents an underestimation of ultimate yields. In taking averages, we also neglect trials where the ion stopped in the unit cell and defects formed at the boundary of the cell. In the trial for which the ion stopped in the unit cell, the number of V_{Si} formed at the aforementioned cutoff was about 24% greater than the average number of V_{Si} formed in the trials where the ion did not stop in the unit cell. Though the estimates represent underestimations, the yield is still far higher than found in experiment[17,18]. The discrepancy cannot be explained by the recombination with Si_i alone, which only accounts for losses of roughly 15% of vacancies, based on our kMC simulations. Given the larger number of C_i, and assuming these defects are distributed similarly to the Si_i defects, we might expect at most an additional loss of 27%. A higher percentage is probably lost from attachment to V_C, which would be energetically favored as explained in more detail below, but the largest contribution is likely charge state variations, due to a Fermi level tuned for example to favor neutral V_{Si}. Fig. 5 (a) shows an ion that stopped in the unit cell. The accumulation of defects near the end of the trajectory is consistent with the creation of a Bragg peak[18]. Further, we see that after an initial nearly stopping collision (at about the position (56,33,61) nm), the ion is still able to travel a significant distance in the crystal, due to the presence of a channel, before actually stopping. These results show that the implantation angle can affect the absolute number of defects created, even though the relative ratio is unaffected, and that a large number of defects are created per incident ion, including through collision cascades. Based on errors calculated from the spread in the data, we conclude that the difference in the number of vacancies created based on implantation angle is indeed significant. However, the limiting case of perfect channeling would also necessarily imply no defects would be formed, so the implantation yield

cannot be a monotonic function of the angle and must reach some maximum at an angle between 10 and 90°. The V_{Si} differs from the NV and other substitutional atom-based qubit candidates in that the emitters are not formed only at the stopping position of the implanted ion (e.g. N^+), but stochastically along the implantation path. Hence, the large number of vacancies formed per incident ion necessitates methods to reduce the density of defects after they are created by ion implantation. Thermal annealing of 4H-SiC is one such method, which we examine next.
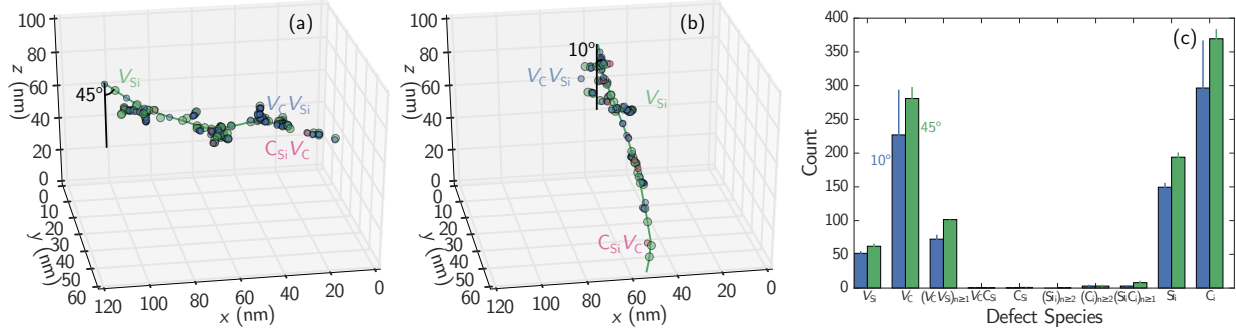

FIG. 5. Sample results of molecular dynamics simulations for trajectories of a Si^{+2} ion, implanted at: (a) 45° and (b) 10° from the c-axis (in the x-z plane) with kinetic energy 70 keV. **(c) Average defect counts for 45° (green) and 10° (blue).**

During high-temperature thermal annealing, V_{Si} defects can recombine with interstitials or transform into $C_{Si}V_C$, another single photon source[33] in 4H-SiC. Both processes reduce the total number of V_{Si}, as desired for lowering V_{Si} density. This requires the diffusion of defects, to which we now turn.

In the high-temperature limit, we obtain an attempt frequency $\nu_0 = 1.7 \times 10^{13}$ s^{-1} by taking into account the degrees of freedom of only the moving Si atom and $\nu_0 = 3.2 \times 10^{13}$ s^{-1} by including the nearest-neighbor C atoms. These attempt frequencies agree well with other results, both theoretical[39], 1.6×10^{13} s^{-1}, and experimental[25], 2.7×10^{13} s^{-1}. In the following we employ our own result for the attempt frequency, including its temperature dependence, for the case where C atoms that neighbor the moving Si atom are included.

Energy barriers for V_{Si} migration and conversion to $C_{Si}V_C$ are presented in Fig. 6. **We note that the energy barrier is lower when the charge of the defect species (V_{Si} and $C_{Si}V_C$) involved in the conversion is more positive (see Fig. 7). However, considering that the Fermi level has been tuned to the range that favors the presence of V_{Si}^- defects, the $V_{Si}^{+1,+2}$ defects will naturally have higher formation energies in that range than V_{Si}^- and will therefore be present in relatively smaller fraction. Thus, there is a tradeoff: though the barrier for conversion of V_{Si} to $C_{Si}V_C$ decreases for increasing charge, the formation**

energy of V_{Si} increases as we move farther away from the -1 charge state (assuming we are in the appropriate Fermi level range that favors V_{Si}^-), lowering the number of species able to make the transition. The fact that the barrier to diffusion of V_{Si} decreases as the charge state becomes more negative can be rationalized by passivation of dangling bonds when electrons are added to the defect.
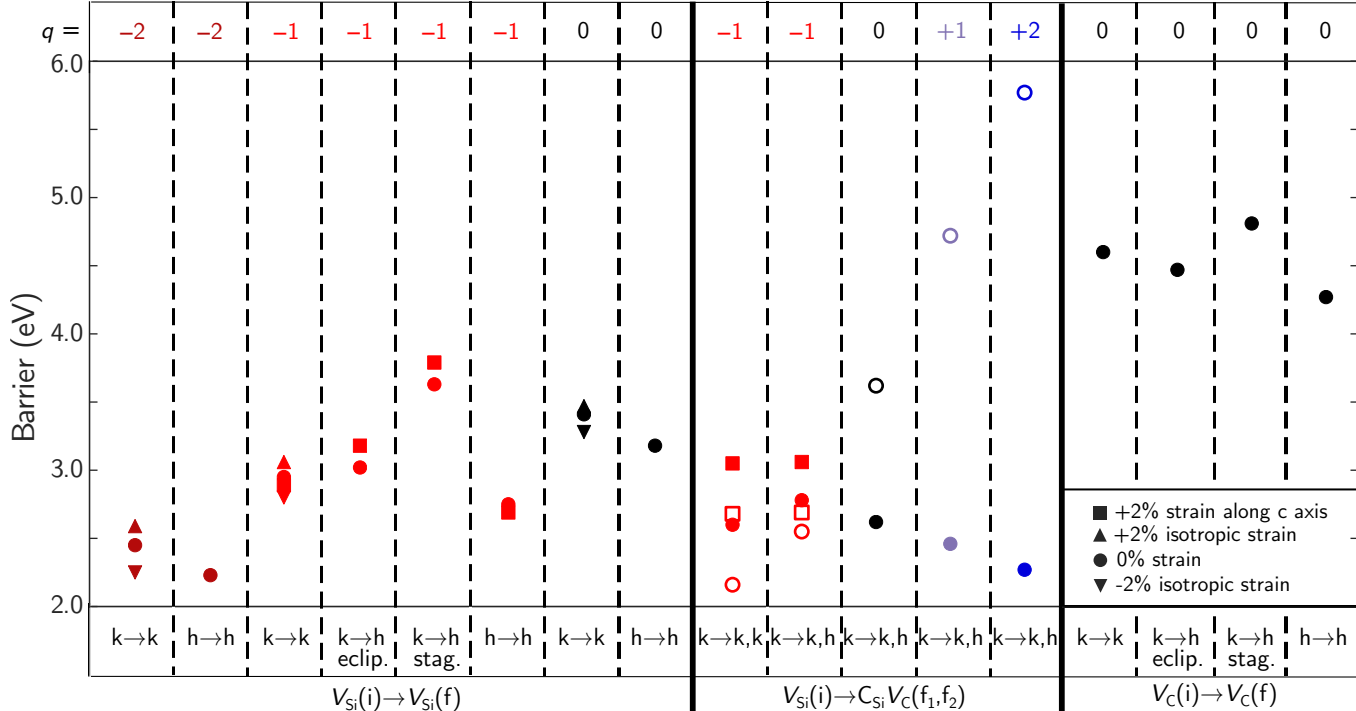

FIG. 6. The barriers for select transitions between defect states. The abbreviation "stag." denotes staggered and "eclip." denotes eclipsed configurations, as defined in Fig. 2. The transition is in-plane and eclipsed when neither eclipsed nor staggered is indicated for a transition between the same species. The lattice site for the initial and final species in the transition is indicated as either hexagonal (h) or cubic (k). The forward (backward) barriers are indicated with filled (empty) symbols. Backward barriers are not shown for differences less than 5%. Black indicates neutral charge, purple/red indicate ± 1 charge and blue/maroon indicate ± 2 charge.

In order to gain greater control over the movement and transformation of the V_{Si} defect during thermal annealing, we explore the dependence of the energy barrier on strain (see Fig. 6). Essentially, if we reduce the displacement of V_{Si} from its initial to its final configuration, the barrier will be lowered, though this argument is not general and applies specifically to vacancy diffusion. This can be achieved by applying strain such that the final and initial positions of V_{Si} are brought closer together. If we apply tensile strain parallel to c-axis, due to the Poisson's ratio, the barrier for in-plane transitions is reduced while the barrier for transitions with a significant out-of-plane component is increased. Since the two pathways for V_{Si} to convert to $C_{Si}V_C$ have a significant out-of-plane component, we can similarly reduce this transformation by applying strain.
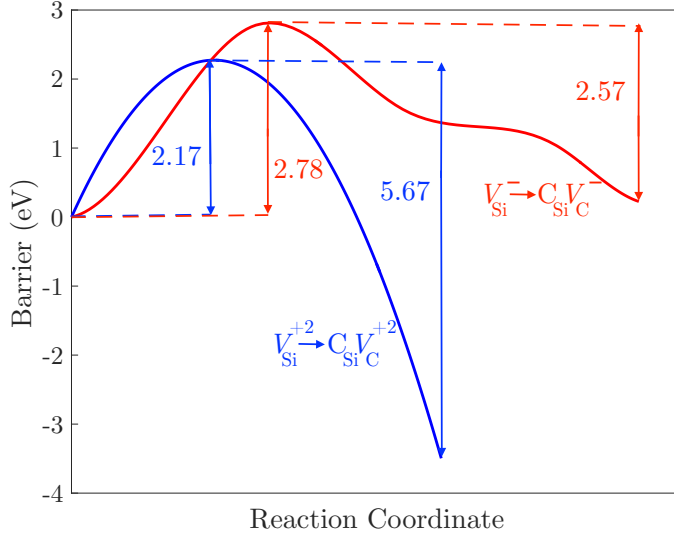
FIG. 7. The barriers for the conversion $V_{\text{Si}} \rightarrow C_{\text{Si}}V_{\text{C}}$ for the charge states -1 (red) and $+2$ (blue). The results are for a 480-atom supercell.

The kMC simulations detailed above yield a diffusion length of 8.4 nm·s^{-1} and a diffusivity of 1.54×10^{-17} m^2·s^{-1} at 1300 K. This differs significantly from earlier results[27] of 0.76 nm·s^{-1} for the diffusion length and 2.9×10^{-19} m^2·s^{-1} for the diffusivity mainly due to the lower energy barriers obtained in our calculations.

From the MD simulations for ion implantation, we obtain the characteristic distances between V_{Si} and interstitial Si atoms, which we used to perform kMC simulations of diffusion at various temperatures to assess timescales for recombination. The results are presented in Fig. 8. For the fit, we observe that, by the construction of the simulation, each atom not in equilibrium has a transition rate that is proportional to $e^{\Delta\phi_i/k_bT}$ and each atom in equilibrium has a transition rate that is proportional to $e^{-\Delta\phi_j/k_bT}$, where $\Delta\phi_i, \Delta\phi_j > 0$ are the differences in the Coulomb potential between the current position of a vacancy and the position one step closer or farther away, respectively, from equilibrium. Here a vacancy is considered to be moving closer to equilibrium if the Coulomb potential at the new location is lower than the potential at the present location while higher potential at the new location implies the vacancy is moving one step farther from equilibrium. We can assume the $\Delta\phi_i$ are all equal ($\Delta\phi_i = \Delta\phi_0$ for all i) and let $\alpha(T) = a(T)e^{\Delta\phi_0/k_bT}$ and that the $\Delta\phi_j$ are all equal ($\Delta\phi_j = \Delta\phi_1$ for all j) and let $\eta(T) = b(T)e^{-\Delta\phi_1/k_bT} - \alpha$, where $a(T)$ and $b(T)$ are coefficients that may depend on temperature and that capture a sum over all i and j, respectively, but which we will assume do not change significantly with time. The cumulative transition rate is proportional to $\alpha(1-x) + (\eta+\alpha)x$, where $x \in [0,1]$ is fraction of atoms in equilibrium and the time is therefore dilated by a factor of $1/(\alpha(1-x) + (\eta+\alpha)x) = 1/(\eta x + \alpha)$. As in any random walk, to first order the

time for a particle to have nonzero probability of reaching a given location is linearly proportional to the distance to the location, so $t \propto d$; we also assume that $x \propto t$, so that $x \propto d$. Rescaling, we have $t = d/(\eta d + \alpha)$. We also expect that V_{Si} would attach to V_{C} as another mechanism for reducing the density of V_{Si}, given that the process would be electrically favored as suggested by Fig. 4, where the energetically favored V_{C} charge states in the $q = -1$ regime for V_{Si} (indicated by the dashed vertical lines) are all positive or zero, therefore they tend to be attracted to the V_{Si}^-. The time scale would be roughly the same as for recombination, so results for that specific process are not presented here.
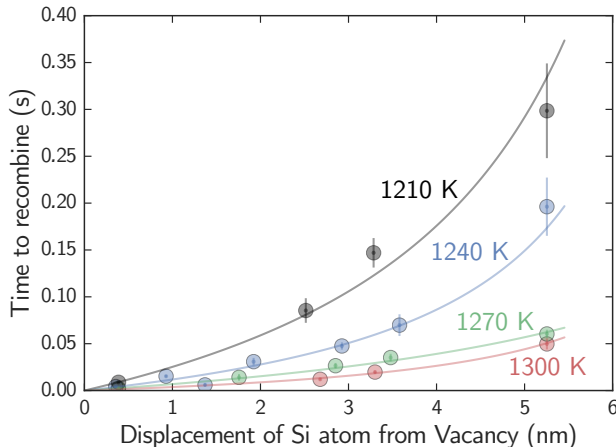

FIG. 8. Recombination time as a function of interstitial Si-V_{Si} distance and temperature. The error bars are the standard error from binning the data into 10 bins for time and distance. The solid-line fit for each temperature is given by $t = d/(\eta d + \alpha)$, where t is the recombination time, d is the displacement and η and α are temperature-dependent parameters described in the text.

Due to the statistical nature of the kMC simulations, many trials are required to accurately reproduce the range of likely diffusion outcomes, particularly for the case of diffusion outcomes with a high level of degeneracy in their probabilities. We therefore explicitly construct the probability map for the position of V_{Si} to verify that the kMC simulations faithfully model the system. Due to the layered structure of 4H-SiC, constructing a full 3D probability map quickly becomes unwieldy. However, given the high energy barriers for out-of-plane motion, if we examine only in-plane migration, we can explicitly calculate the probability of a defect occupying a certain position within the lattice. Let

$$A = \begin{pmatrix} 1 & \frac{1}{\sqrt{3}} \\ 0 & \frac{2}{\sqrt{3}} \end{pmatrix}, \quad R = \begin{pmatrix} \frac{1}{2} & -\frac{\sqrt{3}}{2} \\ \frac{\sqrt{3}}{2} & \frac{1}{2} \end{pmatrix}, \tag{5}$$

12

$$\mathbf{d}_1 = \begin{pmatrix} n_1 \\ 0 \end{pmatrix}, \quad \mathbf{d}_2 = \begin{pmatrix} n_2 \\ 0 \end{pmatrix}, \quad \mathbf{d}_3 = \begin{pmatrix} n_3 \\ m_3 \end{pmatrix}, \tag{6}$$

$$\mathbf{d} = \begin{pmatrix} d_x \\ d_y \end{pmatrix}, \quad \mathbf{N} = \begin{pmatrix} N_1 \\ N_2 \\ N_3 \\ N \end{pmatrix}, \quad N_1 + N_2 + N_3 = N, \tag{7}$$

and p_{xy} be the probability for the V_{Si}^- to migrate to its neighboring in-plane Si lattice site. Here, A is the inverse of the matrix whose columns are the primitive vectors for a hexagonal lattice, R is a matrix that rotates a given set of vectors by $60°$ and $\mathbf{d}_1$, $\mathbf{d}_2$, and $\mathbf{d}_3$ are two-component vectors of integer values related by,

$$\mathbf{d}_3 = AR^2[\mathbf{d} - A^{-1}\mathbf{d}_1 - R^{-1}A^{-1}\mathbf{d}_2]. \tag{8}$$

The probability for V_{Si}^- to be displaced by a vector $(d_x, d_y, 0)$ from its original position (in units of of the in-plane lattice constant) after N time steps is

$$P_{xy}(d_x, d_y, N) = \sum_{N_1=0}^{N} \sum_{N_2=0}^{N-N_1} \sum_{n_1=-N_1}^{N_1} \sum_{n_2=-N_2}^{N_2} \psi(\mathbf{N}, n_1, n_2, \mathbf{d}_3),$$

$$\psi(\mathbf{N}, n_1, n_2, \mathbf{d}_3) = \delta_{0m_3} N! \prod_{i=1}^{3} \frac{(p_{xy})^{N_i}}{\left(\frac{N_i+n_i}{2}\right)! \left(\frac{N_i-n_i}{2}\right)!} \gamma_i. \tag{9}$$

Above, $\gamma_i = 1$ if $\mathrm{mod}(N_i - n_i, 2) = 0$, and 0 otherwise and δ_{0m_3} is the Kronecker delta of the arguments. The increment in time at each step is given by p_{xy}/r_{xy}, where $r_{xy} = D_{xy}/d^2$ is the in-plane transition rate and D_{xy} the in-plane diffusivity. Since the kMC simulations show that out-of-plane transitions are greatly suppressed due to the higher energy barriers compared to in-plane transitions, this simple model does show good agreement with the kMC results. Specifically, we find that the recombination times agree within order of magnitude between the kMC (Fig. 8) and probability map approaches in the low-density limit.

IV. CONCLUSION

Using first-principles calculations for formation energies, diffusion barriers and attempt frequencies, and MD and kMC simulations, and an analytical model, we have studied the thermodynamics and kinetics of V_{Si} in 4H-SiC, from the energetics of formation to its creation through ion implanta-

tion, to its diffusion and recombination during high-temperature annealing. The formation energies obtained are consistent with the relative populations of defects obtained from MD simulations for ion implantation, which also show the influence of implantation angle on the number and types of defects formed. Diffusion barriers for the charge states $-2, -1$ and 0 for V_{Si} show a monotonically increasing barrier with increasing charge. We considered isotropic strain of $-2, 0, +2\%$ and $+2\%$ along the c-axis, and generally found an increase in the diffusion barrier with increasing strain, though the barrier for in-plane transitions is reduced with tensile strain parallel to the c-axis. From these results, we also computed the recombination time of V_{Si} with interstitial Si and developed an analytical model for in-plane migration. This simple model for 2D diffusion in a hexagonal lattice agrees well with the full 3D kMC simulations for the temperatures we have explored. These computational results cover the range of parameters available in the experimental efforts to create and position V_{Si} in 4H-SiC. This information can be useful in guiding integration of V_{Si} within electronic and photonic devices based on 4H-SiC, which is critical for its future applications as a host for solid-state qubits.

[1] R. Schirhagl, K. Chang, M. Loretz, and C. L. Degen, Annual Review of Physical Chemistry **65**, 83 (2014), pMID: 24274702, https://doi.org/10.1146/annurev-physchem-040513-103659.

[2] J. Wrachtrup and F. Jelezko, Journal of Physics: Condensed Matter **18**, S807 (2006).

[3] I. Aharonovich and E. Neu, Advanced Optical Materials **2**, 911 (2014).

[4] A. Lohrmann, B. C. Johnson, J. C. McCallum, and S. Castelletto, Reports on Progress in Physics **80** (2017).

[5] T. Kimoto and J. Cooper, *Fundamentals of Silicon Carbide Technology: Growth, Characterization, Devices and Applications*, Wiley - IEEE (Wiley, 2014).

[6] W. F. Koehl, B. B. Buckley, F. J. Heremans, G. Calusine, and D. D. Awschalom, Nature **479**, 84 EP (2011).

[7] A. L. Falk, B. B. Buckley, G. Calusine, W. F. Koehl, V. V. Dobrovitski, A. Politi, C. A. Zorman, P. X. L. Feng, and D. D. Awschalom, Nature Communications **4**, 1819 (2013).

[8] D. Riedel, F. Fuchs, H. Kraus, S. Väth, A. Sperlich, V. Dyakonov, A. A. Soltamova, P. G. Baranov, V. A. Ilyin, and G. V. Astakhov, Phys. Rev. Lett. **109**, 226402 (2012).

[9] V. A. Soltamov, B. V. Yavkin, D. O. Tolmachev, R. A. Babunts, A. G. Badalyan, V. Y. Davydov, E. N. Mokhov, I. I. Proskuryakov, S. B. Orlinskii, and P. G. Baranov, Phys. Rev. Lett. **115**, 247602 (2015).

[10] M. Widmann, S.-Y. Lee, T. Rendler, N. T. Son, H. Fedder, S. Paik, L.-P. Yang, N. Zhao, S. Yang, I. Booker, A. Denisenko, M. Jamali, S. A. Momenzadeh, I. Gerhardt, T. Ohshima, A. Gali, E. Janzén, and J. Wrachtrup, Nat Mater **14**, 164 (2015).

[11] H. Kraus, V. A. Soltamov, D. Riedel, S. Vath, F. Fuchs, A. Sperlich, P. G. Baranov, V. Dyakonov, and G. V. Astakhov, Nat. Phys. **10**, 157 (2014).

[12] O. O. Soykal, P. Dev, and S. E. Economou, Phys. Rev. B **93**, 081207 (2016).

[13] O. O. Soykal and T. L. Reinecke, Phys. Rev. B **95**, 081405 (2017).

[14] M. Widmann, S.-Y. Lee, T. Rendler, N. T. Son, H. Fedder, S. Paik, L.-P. Yang, N. Zhao, S. Yang, I. Booker, A. Denisenko, M. Jamali, S. A. Momenzadeh, I. Gerhardt, T. Ohshima, A. Gali, E. Janzén, and J. Wrachtrup, Nature Materials **14**, 164 EP   (2014).

[15] D. O. Bracher, X. Zhang, and E. L. Hu, Proceedings of the National Academy of Sciences **114**, 4060 (2017), http://www.pnas.org/content/114/16/4060.full.pdf.

[16] J. Wang, Y. Zhou, X. Zhang, F. Liu, Y. Li, K. Li, Z. Liu, G. Wang, and W. Gao, Phys. Rev. Applied **7**, 064021 (2017).

[17] J. Wang, X. Zhang, Y. Zhou, K. Li, Z. Wang, P. Peddibhotla, F. Liu, S. Bauerdick, A. Rudzinski, Z. Liu, *et al.*, ACS Photonics **4**, 1054 (2017).

[18] H. Kraus, D. Simin, C. Kasper, Y. Suda, S. Kawabata, W. Kada, T. Honda, Y. Hijikata, T. Ohshima, V. Dyakonov, and G. V. Astakhov, Nano Letters **17**, 2865 (2017), pMID: 28350468, https://doi.org/10.1021/acs.nanolett.6b05395.

[19] F. Fuchs, B. Stender, M. Trupke, D. Simin, J. Pflaum, V. Dyakonov, and G. V. Astakhov, Nature Communications **6**, 7578 EP   (2015).

[20] M. Niethammer, M. Widmann, S.-Y. Lee, P. Stenberg, O. Kordina, T. Ohshima, N. T. Son, E. Janzén, and J. Wrachtrup, Phys. Rev. Applied **6**, 034001 (2016).

[21] G. Kresse and J. Hafner, Phys. Rev. B **47**, 558 (1993).

[22] G. Kresse and J. Furthmüller, Phys. Rev. B **54**, 11169 (1996).

[23] G. Kresse and D. Joubert, Phys. Rev. B **59**, 1758 (1999).

[24] J. P. Perdew, K. Burke, and M. Ernzerhof, Phys. Rev. Lett. **77**, 3865 (1996).

[25] M. E. Levinshtein, S. L. Rumyantsev, and M. S. Shur, *Properties of Advanced Semiconductor Materials: GaN, AlN, InN, BN, SiC, SiGe* (John Wiley & Sons, Inc., New York, 2001).

[26] D. Vinichenko, M. G. Sensoy, C. M. Friend, and E. Kaxiras, arXiv:1701.02521v1 [cond-mat.mes-hall] (2017).

[27] X. Wang, M. Zhao, H. Bu, H. Zhang, X. He, and A. Wang, Journal of Applied Physics **114**, 194305 (2013), http://dx.doi.org/10.1063/1.4832457.

[28] S. Plimpton, Journal of Computational Physics **117**, 1 (1995).

[29] S. N. Laboratories, "LAMMPS Molecular Dynamics Simulator," (2018), http://lammps.sandia.gov.

[30] J. Tersoff, Phys. Rev. B **37**, 6991 (1988).

[31] J. F. Ziegler, J. P. Biersack, and U. Littmark (Pergamon Press, New York, 1985).

[32] A. F. Voter, "Introduction to the Kinetic Monte Carlo Method," in *Radiation Effects in Solids*, edited by K. E. Sickafus, E. A. Kotomin, and B. P. Uberuaga (Springer Netherlands, Dordrecht, 2007) pp. 1–23.

[33] S. Castelletto, B. C. Johnson, V. Ivády, N. Stavrias, T. Umeda, A. Gali, and T. Ohshima, Nat Mater **13**, 151 (2014).

[34] K. Szász, V. Ivády, I. A. Abrikosov, E. Janzén, M. Bockstedte, and A. Gali, Phys. Rev. B **91**, 121201 (2015).

[35] N. T. Son, X. T. Trinh, L. S. Løvlie, B. G. Svensson, K. Kawahara, J. Suda, T. Kimoto, T. Umeda, J. Isoya, T. Makino, T. Ohshima, and E. Janzén, Phys. Rev. Lett. **109**, 187603 (2012).

[36] T. Umeda, J. Isoya, N. Morishita, T. Ohshima, and T. Kamiya, Phys. Rev. B **69**, 121201 (2004).

[37] T. Umeda, Y. Ishitsuka, J. Isoya, N. T. Son, E. Janzén, N. Morishita, T. Ohshima, H. Itoh, and A. Gali, Phys. Rev. B **71**, 193202 (2005).

[38] J. Coutinho, V. J. B. Torres, K. Demmouche, and S. Öberg, Phys. Rev. B **96**, 174105 (2017).

[39] E. Rauls, T. Frauenheim, A. Gali, and P. Deák, Phys. Rev. B **68**, 155208 (2003).

[40] J. Towns, T. Cockerill, M. Dahan, I. Foster, K. Gaither, A. Grimshaw, V. Hazlewood, S. Lathrop, D. Lifka, G. D. Peterson, R. Roskies, J. R. Scott, and N. Wilkins-Diehr, Computing in Science & Engineering **16**, 62 (2014).